

RESEARCH ARTICLE

10.1002/2015JD023302

Key Points:

- Increasing solar luminosity will render the Earth uninhabitable within ~2 Gyr
- A radiative-convective transition marks the onset of a moist greenhouse
- A runaway greenhouse may never occur, precluded by rapid water loss

Correspondence to:

E. T. Wolf,
eric.wolf@colorado.edu

Citation:

Wolf, E. T., and O. B. Toon (2015), The evolution of habitable climates under the brightening Sun, *J. Geophys. Res. Atmos.*, 120, 5775–5794, doi:10.1002/2015JD023302.

Received 24 FEB 2015

Accepted 22 MAY 2015

Accepted article online 16 JUN 2015

Published online 25 JUN 2015

The evolution of habitable climates under the brightening Sun

E. T. Wolf¹ and O. B. Toon¹
¹Department of Atmospheric and Oceanic Sciences, Laboratory for Atmospheric and Space Physics, University of Colorado, Boulder, Colorado, USA

Abstract On water-dominated planets, warming from increased solar insolation is strongly amplified by the water vapor greenhouse feedback. As the Sun brightens due to stellar evolution, Earth will become uninhabitable due to rising temperatures. Here we use a modified version of the Community Earth System Model from the National Center for Atmospheric Research to study Earth under intense solar radiation. For small ($\leq 10\%$) increases in the solar constant (S_0), Earth warms nearly linearly with climate sensitivities of $\sim 1 \text{ K}/(\text{W m}^{-2})$ and global mean surface temperatures below 310 K. However, an abrupt shift in climate is found as the solar constant is increased to $+12.5\% S_0$. Here climate sensitivity peaks at $\sim 6.5 \text{ K}/(\text{W m}^{-2})$, while global mean surface temperatures rise above 330 K. This climatic transition is associated with a fundamental change to the radiative-convective state of the atmosphere. Hot, moist climates feature both strong solar absorption and inefficient radiative cooling in the low atmosphere, thus yielding net radiative heating of the near-surface layers. This heating forms an inversion that effectively shuts off convection in the boundary layer. Beyond the transition, Earth continues to warm but with climate sensitivities again near unity. Conditions conducive to significant water loss to space are not found until $+19\% S_0$. Earth remains stable against a thermal runaway up to at least $+21\% S_0$, but at that point, global mean surface temperatures exceed 360 K, and water loss to space becomes rapid. Water loss of the oceans from a moist greenhouse may preclude a thermal runaway.

1. Introduction

Earth's climate is dominated by water. While water in its liquid phase is believed essential for planetary habitability, the over abundance of water in its solid or gaseous phases can create catastrophic instabilities in the climate system. The high reflectivity of snow and water ice at visible wavelengths is a cause for the sea ice albedo feedback and runaway glaciations. Geologic evidence indicates that episodes of low-latitude glaciation have likely occurred on Earth in the distant past [Evans *et al.*, 1997; Young *et al.*, 1998; Hoffman *et al.*, 1998]. The high infrared (IR) opacity of water in its vapor phase is cause for the water vapor greenhouse feedback as well as both moist and runaway greenhouses. Venus succumbed to the water vapor greenhouse feedback billions years ago [Pollack, 1971; Donahue *et al.*, 1982]. Under the continually brightening Sun, a Venusian fate likely awaits Earth.

The well-established standard solar model predicts that all stars gradually brighten during their main sequence lifetimes [Gough, 1981; Ribas, 2009]. Earth will be subjected to larger doses of solar energy in the future [Guinan and Ribas, 2002]. Presently our Sun grows brighter by 1% every $\sim 110 \text{ Myr}$. This trend will continue for another $\sim 5 \text{ Gyr}$ before the Sun enters its red giant phase, whereupon its atmosphere will expand outward to near the present orbit of Earth [Schröder and Smith, 2008]. Earth will inevitably transition into hotter climates that are beyond the realm of those experienced by humans to date.

Warming climates are thought to transition through two distinct phases: the moist greenhouse and the runaway greenhouse. The term "moist greenhouse" was first coined by Towe [1981] in reference to hot water-rich atmospheres that are speculated for the Hadean Earth, more than 4 Gyr ago. Towe postulated that water vapor mixing ratios could become significant up to high altitudes, where H_2O is prone to photolytic destruction and subsequent loss (of hydrogen) to space. Later, Kasting *et al.* [1984b] and Kasting [1988] refined the definition of the moist greenhouse in terms of water loss and planetary habitability. Kasting *et al.* [1984b] predict that if the water vapor volume mixing ratio with respect to moist air exceeds $10^{-3} \text{ kg kg}^{-1}$ in the stratosphere, Earth's entire inventory of water will be lost to space within the present age of the Earth ($\sim 4.6 \text{ Ga}$), thus terminating conventional habitability. One-dimensional radiative-convective

calculations predict that stratospheric water vapor mixing ratios of $\sim 3 \times 10^{-3}$ can occur if the global mean surface temperature reaches 340 K, under the assumptions of water vapor saturation and a 200 K isothermal stratosphere [Kasting, 1988]. This description is often taken as the standard threshold for a moist greenhouse climate. A moist greenhouse is generally believed to precede a runaway greenhouse in the evolutionary sequence of warming terrestrial atmospheres. While a moist greenhouse is climatologically stable, unlike a runaway greenhouse, the potential for rapid water loss makes it the more proximal boundary to the inner edge of the habitable zone [Kasting et al., 1993; Kopparapu et al., 2013].

The runaway greenhouse differs sharply from the moist greenhouse. In a runaway greenhouse, the entire inventory of water on the planet is contained in the atmosphere as vapor and cloud. For Earth's present inventory of water, a runaway greenhouse would have a surface pressure of several hundred bars and surface temperatures well in excess of the critical temperature for water [Kasting, 1988]. A transition to a runaway greenhouse is marked by a radiative instability where outgoing longwave radiation reaches an asymptotic limit due to overwhelming water vapor opacity in the IR [Simpson, 1927; Komabayashi, 1967; Ingersoll, 1969; Nakajima et al., 1992; Goldblatt et al., 2013]. Outgoing longwave radiation can no longer increase to match rising solar insolation, and thus climate warms uncontrollably until all surface water has evaporated and mean surface temperatures exceed ~ 1600 K. At this point, thermal emission through the $4 \mu\text{m}$ water vapor window becomes strong enough to stabilize climate [Goldblatt et al., 2013]. Note that an atmosphere in runaway would also undergo rapid water loss to space.

Recently the simulation of warming climate has been approached with three-dimensional climate models of various heritages. Abe et al. [2011] used the atmospheric general circulation model 5.4g from the Center for Climate System Research, University of Tokyo, to study desert planets. Leconte et al. [2013a] used the Laboratoire de Météorologie Dynamique Generic (LMDG) climate model from the Laboratoire de Météorologie Dynamique, Paris, France, to study tidally locked, water-limited land planets inside the classical inner edge of the habitable zone. Again, using LMDG, Leconte et al. [2013b] found that Earth will enter a runaway greenhouse when the solar constant exceeds $+10\%$ S_0 . Interestingly, their results indicate that Earth may not experience a moist greenhouse phase, instead skipping directly to a runaway greenhouse. Their warmest stable simulation has a mean surface temperature of only ~ 335 K and relatively low upper atmospheric water concentrations. Wolf and Toon [2014a], using the Community Atmosphere Model version 3 from the National Center for Atmospheric Research, Boulder, CO, found Earth to be much more resistant to warming, reaching mean surface temperatures of only ~ 313 K at $+15.5\%$ S_0 . However, numerical issues prevented the simulation of hotter climates.

At the present time then, an unsolved problem is whether the Earth will eventually reach a moist greenhouse, a runaway greenhouse, or both. In addition, the values of S_0 at which these transitions occur are not well defined. Here we reexamine warming climate for Earth using an updated three-dimensional climate model (see section 2). Model improvements allow us to study more carefully the properties of true moist greenhouse atmospheres.

2. Model Description

2.1. Overview

We use the Community Earth System Model (CESM) version 1.2 from the National Center for Atmospheric Research in Boulder, CO. Here we configure CESM using the Community Atmosphere Model version 4 (CAM4) with a finite volume dynamical core [Lin and Rood, 1996]. CAM4 has been validated extensively for the present-day climate [Marsh et al., 2013]. We use $4^\circ \times 5^\circ$ horizontal resolution with 45 vertical levels extending up to a model top of ~ 0.2 mbar. Our configuration offers significantly greater vertical resolution than does the standard CAM4 configuration which uses only 26 vertical levels up to a model top of ~ 3 mbar. While our horizontal resolution is kept relatively coarse to promote computational efficiency, it is generally comparable or slightly better than that used in other 3-D studies of planetary atmospheres. We assume a continental configuration and land coverage identical to the present-day Earth, except that permanent glacial ice sheets found over Greenland, Antarctica, and the Himalaya have been replaced with bare soil. However, sea ice and snow can still accumulate if atmospheric conditions dictate. Orbital-rotational parameters (obliquity, rotation rate, eccentricity, and length of year) and the wavelength dependence of the incident solar spectrum are also held identical to the present-day Earth. We use a

thermodynamic “slab” ocean model with specified (but seasonally varying) internal ocean heat fluxes that duplicate present-day patterns of ocean heat transport [Bitz *et al.*, 2012]. We have included a correlated k radiative transfer code that has been designed with deep paleoclimate and exoplanetary atmospheres in mind [Wolf and Toon, 2013]. We use physics and radiative time steps of 30 min, with 32 dynamical substeps per physics time step. We use a larger than standard value for the frequency of dynamical substepping in order to ensure numerical stability for our hottest simulations.

2.2. General Assumptions

The atmosphere is assumed to consist only of N_2 , CO_2 , and H_2O . Oxygen, ozone, methane, trace gas species, and the direct radiative effect of aerosols are excluded. The total pressure of the atmosphere is given by

$$P_{\text{tot}} = P_{N_2} + P_{CO_2} + P_{H_2O} \quad (1)$$

where P_x is the partial pressure of each gaseous component, respectively. N_2 and CO_2 are noncondensable “dry” gases, and thus their amounts are fixed in all simulations. The global mean dry surface pressure is 982.88 mbar, with CO_2 comprising 367 ppmv of the dry fraction. Note that the dry pressure is equal to that of the modern atmosphere despite the removal of O_2 (21% of the modern atmosphere). N_2 has been added to make up for the mass lost by removing the O_2 . H_2O is a condensable species and thus is spatially and temporally varying. H_2O can add mass to the atmosphere [Neale *et al.*, 2010]. The molecular weight of dry air and the specific heat of dry air are set by the relative amounts of CO_2 and N_2 . The present-day solar constant is assumed to be 1361.27 W m^{-2} .

2.3. Radiative Transfer

We use the correlated k radiative transfer scheme first described in Wolf and Toon [2013]. The scheme uses k coefficients derived from the HITRAN 2004 spectroscopic database using the line by line radiative transfer model (LBLRTM) developed by Atmospheric and Environmental Research Inc. in Lexington, MA [Clough *et al.*, 2005]. We use 28 spectral intervals that range from 10 to $50,000 \text{ cm}^{-1}$ to include both solar and terrestrial radiation. We have expanded the temperature and pressure ranges in our k coefficient tables to include pressures up to 10 bar and temperatures up to 520 K, well covering the bounds of this study. Water vapor foreign broadening coefficients have been combined with spectral k coefficients due to their mutual linear dependence on abundance [Mlawer *et al.*, 1997]. Overlapping molecular absorption is treated using the amount-weighted scheme of Shi *et al.* [2009]. The foreign broadening gas is N_2 . Water vapor self-continuum coefficients are derived from the MT_CKD version 2.5 continuum model [Clough *et al.*, 2005]. CO_2 foreign broadening is also taken from MT_CKD, with the assumption of N_2 as the broadening gas. The self-broadened continuum for CO_2 , which is not included in MT_CKD, is assumed to be 1.3 times the foreign broadened continuum to account for the greater broadening efficiency of CO_2 versus N_2 following Kasting *et al.* [1984a] and Halevy *et al.* [2009]. N_2 self-broadening coefficients are included from Borysow and Frommhold [1986]. Rayleigh scattering is calculated for N_2 , CO_2 , and H_2O following Vardavas and Carver [1984] with coefficients from Allen [1973]. The model uses a standard two-stream radiative transfer solver with multiple scattering from Toon *et al.* [1989].

When simulating hot moist atmospheres, the use of HITRAN2004 leads to an underestimation of absorbed solar radiation (ASR) and an overestimation of outgoing longwave radiation (OLR) compared with the HITEMP2010 line list [Goldblatt *et al.*, 2013]. Here our hottest simulation has a global mean surface temperature of $\sim 363 \text{ K}$, while local and seasonal temperature maxima can marginally exceed 400 K. In this temperature range, clear-sky flux errors caused by using HITRAN2004 amount to at worst $\sim 2\%$ for ASR and $\sim 0.5\%$ for OLR. For temperatures below 360 K, errors in ASR are $\leq 0.6\%$. The presence of clouds and subsaturated regions should further mute the differences found between HITRAN2004 and HITEMP2010 calculations. We feel that these margins of error are acceptable for this study.

2.4. Moist Physics

Over the past two decades, cloud modeling has advanced tremendously such that realistic three-dimensional cloud fields can be considered. Prognostic bulk microphysical parameterizations for condensation, precipitation, and evaporation control atmospheric water vapor, liquid cloud, and ice cloud condensate fields [Rasch and Kristjánsson, 1998]. Deep convection (i.e., moist penetrative) is treated using the parameterization of Zhang and McFarlane [1995]. This scheme has been further modified to include

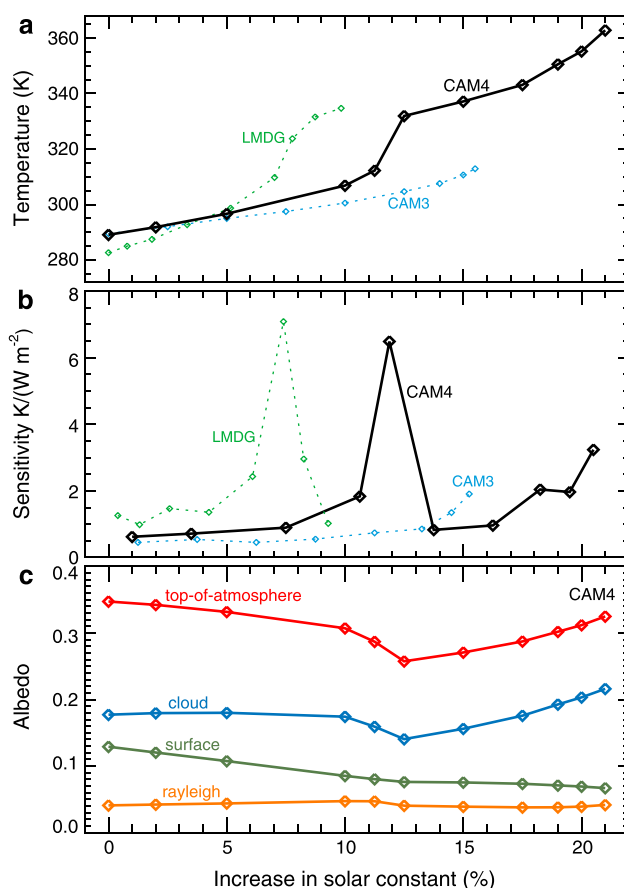


Figure 1. Global and annual (a) mean surface temperature, (b) climate sensitivity, and (c) albedo versus increasing solar constant. Data labeled LMDG is from *Leconte et al.* [2013b]. Data labeled CAM3 is from *Wolf and Toon* [2014a]. Data labeled CAM4 is from this study.

clouds at all altitudes depend on the relative humidity and the pressure level. Over oceans and sea ice, liquid cloud droplet effective radii are assumed to be $14\text{ }\mu\text{m}$, while over land they vary from 8 to $14\text{ }\mu\text{m}$ dependent on the ambient temperature. Ice particle effective radii follow a strictly temperature-dependent parameterization and can vary in size from a few tenths to a few hundred microns [Neale et al., 2010]. A typical ice cloud in the model has an effective radius of $\sim 50\text{ }\mu\text{m}$ at air temperatures of 240 K and $\sim 20\text{ }\mu\text{m}$ at air temperatures of 200 K .

The study of *Wolf and Toon* [2014a] was truncated at mean surface temperatures no higher than $\sim 313\text{ K}$ due to numerical instabilities. This issue has now been corrected. Previously, the entropy closure calculation within the deep convection scheme failed to converge for hot atmospheres. The code has now been updated (courtesy C.A. Shields) to use the more robust numerical approach of *Brent* [1973].

3. Results

3.1. Evolution of Climate

We first conduct a “present-day” control simulation with the solar constant at 1361.27 W m^{-2} . This simulation yields a global mean surface temperature (T_s) of 289.1 K . Our result is reasonably close to published high-resolution simulations using unaltered CAM4, which predict $T_s = 288.2\text{ K}$ averaged over the 1986 to 2005 time period [Marsh et al., 2013]. This small difference is not unexpected considering the divergence of our model construction compared with the off-the-shelf version of CAM4 (see section 2).

Starting from our present-day simulation, we then incrementally increase the solar constant. Figure 1 shows the evolution of global mean surface temperature, climate sensitivity (λ), and albedo versus percent increase

convective momentum transport [Richter and Rasch, 2008] and dilute entraining plumes [Raymond and Blyth, 1986, 1992]. The deep convection scheme utilizes a plume ensemble approach, where convective updrafts and downdrafts occur wherever the lower atmosphere is found to be conditionally unstable. Shallow convective overturning is treated by the parameterization of *Hack* [1994]. CAM4 self-consistently accounts for changing atmospheric pressures due to changing water vapor amounts in each grid cell. The total grid cell water vapor tendency includes contributions from advection, convection, turbulent mixing, and large-scale stable condensation and evaporation. CAM4 uses virtual temperature corrections to account for the density variation between moist and dry air.

Cloud fractions are diagnosed for three separate genres. Marine stratus cloud fractions depend on the stratification of the atmosphere between the surface and the 700 mbar level. Convective cloud fractions depend on the stability of the atmosphere and the upward convective mass flux. Layered

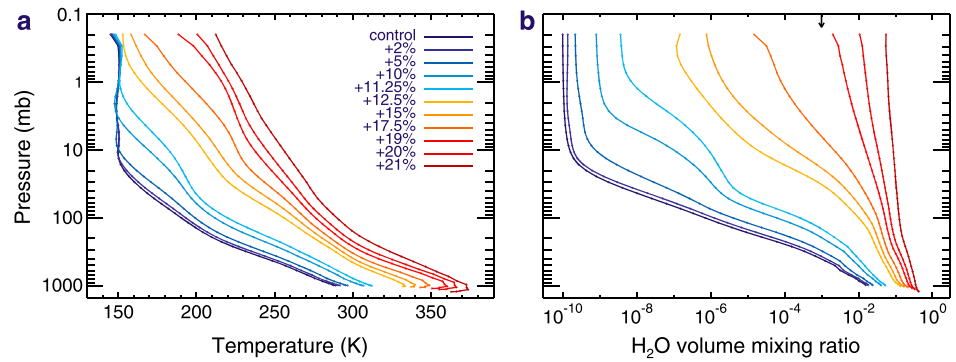


Figure 2. (a) Global mean vertical profiles of temperature and (b) H₂O volume mixing ratio relative to moist air. The arrow in Figure 2b signifies the upper atmospheric H₂O mixing ratio threshold for the onset of significant water loss to space. The blue lines are for temperate simulations ($T_s < 315$ K). The orange and red lines are for moist greenhouse simulations ($T_s > 330$ K). Note that the vertical profiles of temperature include the global mean surface temperature as their lowest data point.

in the solar constant above the present day. Climate sensitivity is the change in mean surface temperature for a given change in radiative forcing. Thus, for changes to the solar constant,

$$\lambda = \frac{\Delta T_s}{\Delta S(1 - A_p)/4} \quad (2)$$

where ΔT_s is the incremental change in global mean surface temperature, ΔS is the incremental change in solar constant in W m^{-2} , and A_p is the top-of-atmosphere (TOA) albedo before the increase in solar constant is applied. Results are shown from this study and recent analogous 3-D studies of a warming Earth. We designate “CAM4” for new results from this study, “CAM3” for results presented in *Wolf and Toon* [2014a], and “LMDG” for results presented in *Leconte et al.* [2013b] using the LMD Generic global climate model. CAM3 and CAM4 have been modified from their original forms as described in *Wolf and Toon* [2014a] and in section 2 here. Climate sensitivity is plotted on a staggered x coordinate grid, located at the midpoint of each incremental change in solar constant.

In the CAM4 simulation, climate at first warms modestly with $\lambda \sim 1 \text{ K}/(\text{W m}^{-2})$ for increases to the solar constant of $\leq 10\%$. However, further increases to the solar constant trigger an abrupt shift into a hotter climatic regime. As the solar constant is increased from +11.25% S_0 to +12.5% S_0 , mean surface temperatures rise from 312.2 K to 331.9 K despite an incremental TOA solar forcing of only $+3.0 \text{ W m}^{-2}$, yielding a sharp maximum in climate sensitivity of $\sim 6.5 \text{ K}/(\text{W m}^{-2})$ (Figures 1a and 1b). The sharp climatic transition is accompanied by minima in global mean cloud and TOA albedos (Figure 1c). Immediately beyond the transition, climate continues to warm but again with modest sensitivities as the cloud albedo increases, mitigating warming. Variations in the Rayleigh scattering albedo remain small. The surface albedo continuously declines, first due to the melting of snow and ice, and then due to spectral effects. Land surface albedos are split into visible and near-IR bands at $\sim 0.76 \mu\text{m}$, with the visible albedo being half that of the near-IR. Water vapor absorption is stronger in the near-IR than the visible, thus for progressively hotter climates, the solar flux incident upon the ground becomes relatively enriched at visible wavelengths and therefore the broadband surface albedo subtly declines.

Interestingly, both CAM4 and LMDG results display a qualitatively similar shape for temperature and climate sensitivity curves (Figures 1a and 1b). Both models exhibit a sharp peak followed by weakening climate sensitivity rather than an immediate onset of a thermal runaway upon the initial phase of rapid warming. In order to produce this sharp peak in sensitivity, some process must (at least temporarily) interrupt the water vapor greenhouse feedback. Maxima in climate sensitivity are offset between CAM4 and LMDG, occurring between +11.25% and +12.5% S_0 in CAM4 and between +7% and +7.8% S_0 in LMDG. LMDG is inherently a more sensitive model, becoming hotter, sooner than does CAM4 (Figure 1b). The CAM3 results suffer from numerical instabilities before a transition to a hotter climate can occur; thus, no spike in climate sensitivity is evident. CAM3 is less sensitive than both CAM4 and LMDG. On first order, model differences can be explained by differences in the clouds (see section 3.4).

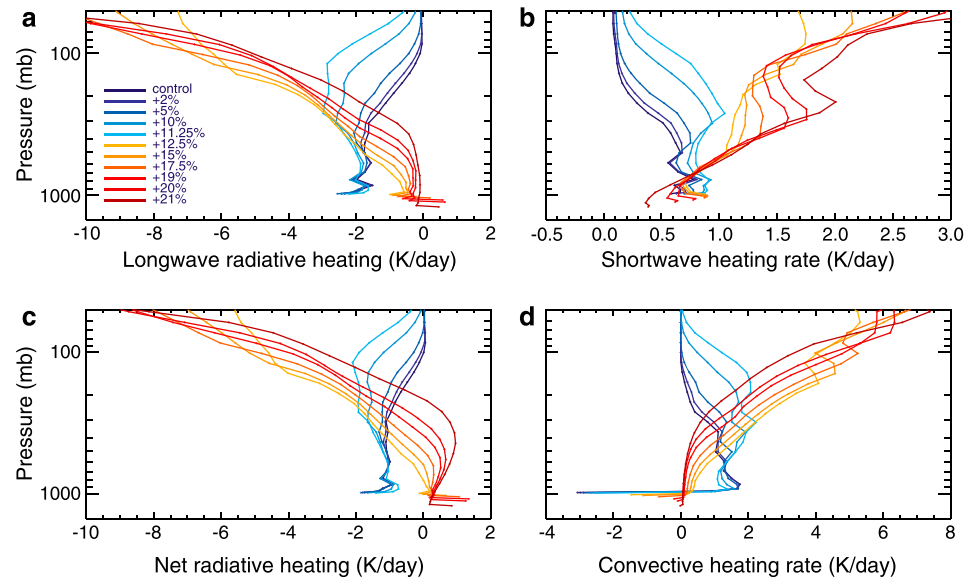


Figure 3. Global mean vertical profiles for (a) longwave heating rate, (b) shortwave heating rate, (c) net radiative heating rate, and (d) convective heating rate for the lower atmosphere only. The top of model is not shown. The blue lines are for temperate simulations ($T_s < 315$ K). The orange and red lines are for moist greenhouse simulations ($T_s > 330$ K). The moist greenhouse simulations exhibit a distinctive radiative-convective state.

Figure 2 explores the atmospheric temperature profiles in CAM4, for various values of the solar constant. When S_0 reaches +12.5%, $T_s = 331.9$ K and the H_2O volume mixing ratio at the top of the model (Q_{top}) reaches 1.5×10^{-5} , falling short of the classical definition of the moist greenhouse threshold given by *Kasting* [1988]. (Note that this value is not far from those in the present atmosphere, but today the upper atmosphere is much warmer than the simulations shown in Figure 2 due to ozone heating). However, here we will refer to the +12.5% S_0 , $T_s = 331.9$ K case as the first (i.e., coldest) moist greenhouse atmosphere. The dramatic surface temperature transition illustrated in Figure 1 is accompanied by distinctive changes to the radiative-convective state of the atmosphere (see section 3.2), and thus it stands as a logical demarcation between climatic regimes. The upper atmospheric water vapor threshold for a moist greenhouse of $\geq 10^{-3}$, as defined by *Kasting* [1988], is not reached until the +19% S_0 case, where $T_s = 350.5$ K and $Q_{top} = 2.0 \times 10^{-3}$. Climatologically stable simulations are found with the solar constant reaching up to +21% S_0 and $T_s = 362.8$ K. In this hottest case, $Q_{top} = 5.6 \times 10^{-2}$, and thus water loss may become rapid relative to the rate of solar brightening (see section 4.1).

For increases to the solar constant beyond +21% S_0 we find no converged solutions. Our model begins to experience numerical instabilities within the dynamical core when $T_s > 367$ K. Numerical instabilities can be suppressed by increasing the frequency of dynamical substepping, but this process becomes increasingly inefficient. While $T_s \leq 363$ K, as found here, is sufficient for studying habitable climates, one cannot rule out climatologically stable states existing at hotter temperatures [Goldblatt, 2015]. However, for the chronology of Earth it may not matter whether the climate uncontrollably warms or whether it remains stable beyond our computational limitations. Rapid water loss to space is expected from our hottest atmosphere (+21% S_0 , $T_s = 362.8$ K). In this case the oceans may be lost before the solar constant has appreciably increased further. Loss of the entire oceans would transform Earth forever into a desert planet, limiting water availability, and possibly preventing a runaway greenhouse from ever occurring. Even if a runaway was to occur at some larger value of S_0 , water loss to space would still eventually render Earth a desert planet. While our results leave the door open for climatologically stable states to exist with $T_s > 362.8$ K, such atmospheres become increasingly unstable against water loss to space and thus are increasingly short-lived phenomena. Note that the hottest stable simulation in LMDG is found at +10% S_0 and $T_s = 335$ K, whereupon the thermal limiting flux is reached and presumably a runaway greenhouse is the result [Leconte et al., 2013b].

3.2. Radiative-Convective Transition

As described in section 3.1, when the solar constant is increased to +12.5% S_0 , Earth will abruptly transition into a moist greenhouse. This transition is accompanied by a profound change in the radiative-convective state of the atmosphere, illustrated in Figure 3. The genesis of this change lies in the water vapor greenhouse feedback. As T_s rises above ~ 310 K, the water vapor window region (8–13 μm) closes, and thus the lowest layers of the atmosphere become thermally opaque. Despite continued increases to T_s , the spectrally resolved emitting level of the atmosphere remains between 250 and 300 K and therefore above the surface [Goldblatt *et al.*, 2013]. Radiative cooling becomes stronger high in the atmosphere as the emitting level is pushed upward as climate warms. However, radiative cooling becomes negligible in the low atmosphere because the surface layers can no longer cool directly to space (Figure 3a). Note that Figure 3 shows only the lower part of our model atmospheres. Meanwhile, solar absorption by near-IR water vapor bands causes shortwave radiative heating to become stronger for all layers of the atmosphere except for the bottom most (Figure 3b). Increased attenuation of solar radiation by water vapor aloft increases atmospheric heating while preventing some of the Sun's energy from reaching the surface. However, water vapor is a weaker absorber in the shortwave compared with the longwave. Thus, even with surface water vapor volume mixing ratios of up to ~ 0.4 , as found in our hottest simulation, some solar radiation can still penetrate to the surface to drive heating and evaporation.

Combining the effects of terrestrial and solar radiation, a moist greenhouse atmosphere features net radiative heating in the low atmosphere, as opposed to net radiative cooling which is observed for Earth's present climate and all climates that fall below the moist greenhouse transition (Figure 3c). Net radiative heating in the lower atmosphere creates a permanent near-surface inversion (Figure 2a). The sign change in low-level radiative heating rates and the associated inversions become more pronounced as the atmosphere becomes progressively hotter, increasingly water rich, and thus radiatively opaque.

For moist greenhouse atmospheres, the inversion is overlain by a nearly isothermal layer, creating a stable low atmosphere. For the coldest moist greenhouse with $T_s = 331.9$ K, the inversion and isothermal layer are shallow and weak, extending only to an altitude of ~ 0.4 km with a depth of only ~ 0.5 K on global mean. As temperatures climb, this stable layer grows deeper and stronger. By our hottest simulation ($T_s = 362.8$ K), the inversion and overlying isothermal layer extend to an altitude of ~ 1.7 km with a depth of ~ 10 K.

Near-surface inversions are stronger and onset at a lower solar insolation over ocean compared with over land due to significantly higher relative humidities and thus increased thermal and solar opacities over the oceans. By the time that our hottest simulation is reached, low atmosphere inversions are present everywhere except for a narrow band over the tropics. In Figure 4a, inversions are visible as warm lobes inside closed temperature contours centered at midlatitudes in the low atmosphere of the hottest simulation (fourth column). Seasonally, inversions are strongest over the summer hemisphere. On the present-day Earth, strong inversions occur over the poles during winter. Here large-scale polar inversions are destroyed at the moist greenhouse transition. Inversions do again form over the poles in our hottest simulations but are generally weak.

Earlier studies of hot, moist climates did not find near-surface inversions because the temperature profiles were forced to analytical expressions for the moist adiabat under water-rich conditions, precluding surface inversions from ever forming [Kasting, 1988; Kasting *et al.*, 1993; Kopparapu *et al.*, 2013; Leconte *et al.*, 2013b]. However, near-surface inversions have been noted recently in 1-D modeling studies that remove assumptions fixing the lapse rate to an analytical formula [Wordsworth and Pierrehumbert, 2013; Popp *et al.*, 2015]. We suggest that near-surface inversions are a defining characteristic of the moist greenhouse atmosphere.

The environmental temperature profile has a fundamental affect on convective processes. Figure 5 shows the temperature and lapse rate profile for our hottest simulation versus the dry and moist adiabats. The moist adiabat is approximated here by

$$\Gamma_m = g \frac{1 + \frac{L_v q_v}{RT}}{C_{pd} + \frac{L_v^2 q_v \epsilon}{RT^2}} \quad (3)$$

where g is the acceleration of gravity, L_v is the latent heat of vaporization, R is the gas constant for dry air, C_{pd} is the specific heat of dry air, ϵ is the ratio of water vapor and dry air molecular weights, q_v is the water vapor mass mixing ratio in the layer, and T is the temperature of the layer. We find a qualitatively similar vertical structure as is described in Wordsworth and Pierrehumbert [2013], with a moist greenhouse atmosphere separated into three distinctive convective regions. The inversion layer is absolutely stable against convection.

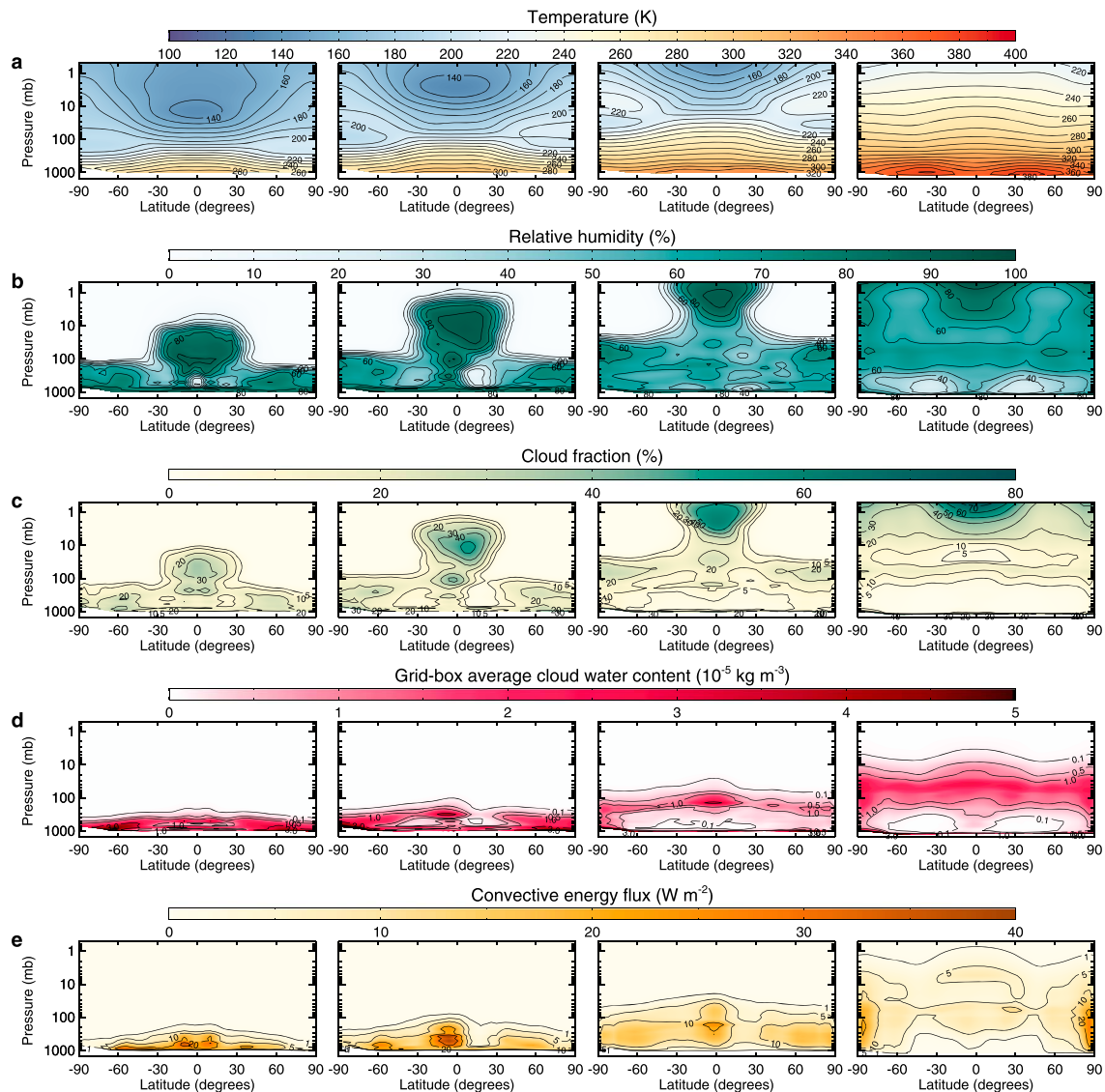


Figure 4. The evolution of (a) zonal mean air temperature, (b) relative humidity, (c) cloud fraction, (d) grid box cloud water content, and (e) convective energy flux. The columns show results for our control simulation +10% S_0 , +12.5% S_0 , and +21% S_0 moving from left to right.

Thus, for moist greenhouse atmospheres, convection in the low atmosphere is suppressed (Figures 3d and 4e). Immediately above the inversion, the atmosphere is dry, having low relative humidities (Figure 4b), few clouds (Figures 4c and 4d), and a lapse rate that exceeds Γ_m . The upper atmosphere (above ~20 km or equivalently ~100 mbar) is moist. The environmental lapse rate follows the moist adiabat closely as cloud condensation takes place over a significant fraction of the atmosphere. In this case the moist adiabat does not trend to the dry value because there is so much water in the atmosphere that latent heat release is important at all levels, unlike in the current atmosphere. Note that the transition from dry to moist regions marks location of the cloud base for the primary cloud deck (Figures 4c and 4d).

Figure 6 illustrates the radiative, convective, and cloud states of our hottest moist greenhouse simulation. The atmosphere is optically thick to both longwave (LW) and shortwave (SW) radiation beginning near the top of the dry region, indicated by the change in slope of the net radiative fluxes near 20 km. Figure 7a shows that this atmosphere contains the equivalent of about 2.5 m of precipitable water in the vapor phase. While convective energy fluxes are shut off in the boundary layer due to the inversion, solar radiation is absorbed near the dry/moist layer interface and acts as an energy source for driving upper level convection. For moist

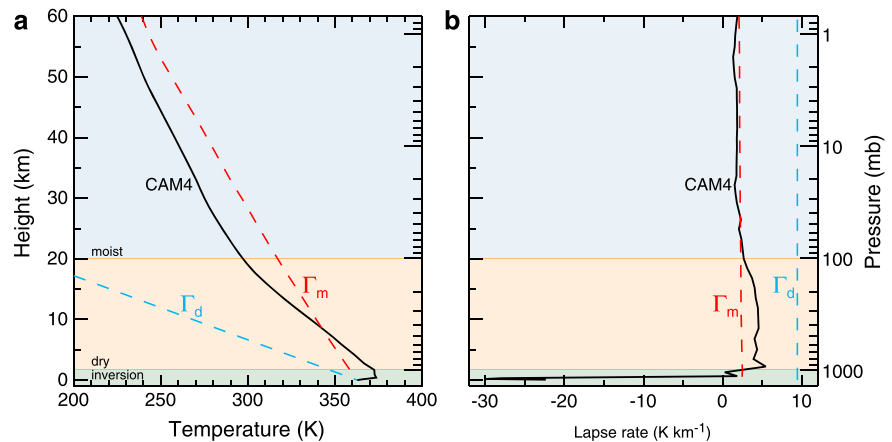


Figure 5. (a) Global mean temperature profile and (b) lapse rate compared to the moist (Γ_m) and dry (Γ_d) adiabats for our hottest simulation ($T_s = 362.8$ K at $+21\%$ S_0). A moist greenhouse atmosphere is divided into three distinct convective regions: inversion layer, dry, and moist. The surface temperature is included as the lowest point in the temperature profile.

greenhouse atmospheres, convective energy fluxes reach their peak values at the bottom of the moist region, coincident with the primary cloud deck.

Convection aids thermal radiation in transporting energy from the surface to higher layers of the atmosphere [Ramanathan and Coakley, 1978]. For simulations of present-day climate, convection cools the surface by 3.1 K d^{-1} on global mean (Figure 3d). As climate warms to 312.2 K at $+11.25 S_0$ (our warmest simulated climate below the moist greenhouse transition), convective surface cooling gradually reduces to 2.5 K d^{-1} . However, as Earth transitions from temperate conditions to a moist greenhouse (i.e., with an inversion), surface cooling via convection abruptly drops to 1.5 K/d . As inversions grow stronger for progressively hotter simulations, boundary layer convection, and thus convective cooling of the planet surface, effectively vanishes. As climate switches into the moist greenhouse state, the surface can neither efficiently cool radiatively nor convectively, combining to spur abrupt warming as shown in Figure 1.

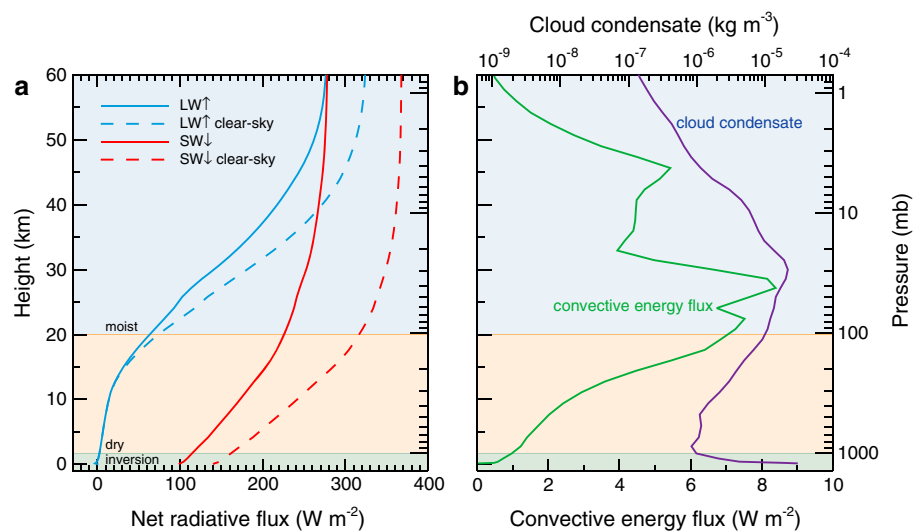


Figure 6. Global mean net radiative fluxes along with convective and cloud properties for our hottest simulation ($T_s = 362.8$ K at $+21\%$ S_0). (a) The net upwelling longwave (LW) flux and the net downwelling shortwave (SW) flux. The full-sky (i.e., with cloud) fluxes are the solid lines. The dashed lines are for clear-sky radiative fluxes. (b) The convective energy flux (bottom axis) and the cloud condensate amount (top axis).

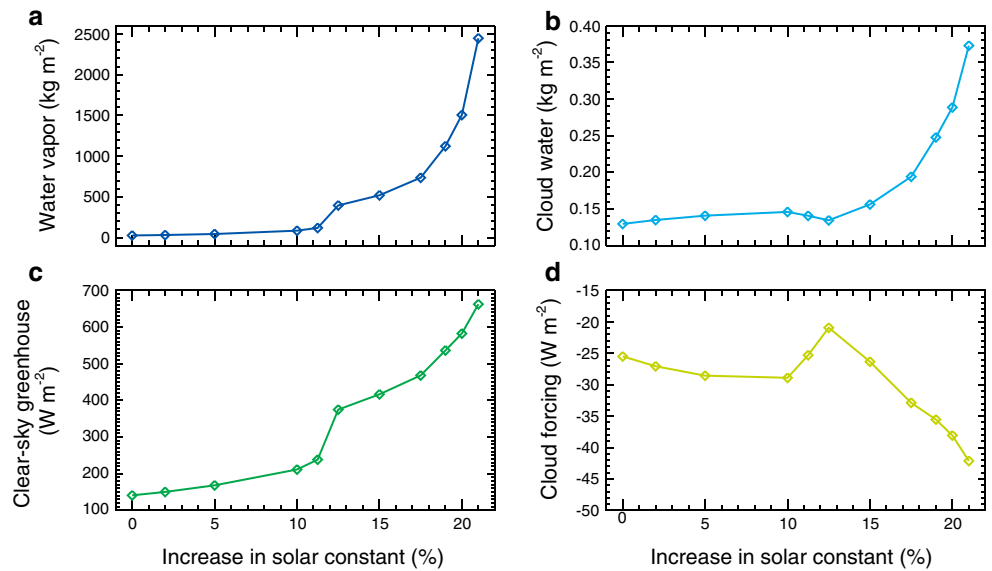


Figure 7. Global mean (a) water vapor column, (b) cloud water column, (c) clear-sky greenhouse effect, and (d) cloud forcing versus increasing solar constant.

3.3. Clouds and Water

Moist greenhouse atmospheres feature two cloud layers (Figures 4c and 4d). The first is a widespread fog that blankets the planet surface, just below the inversion layer, where the atmosphere is in direct contact with the oceans and relative humidities remain high. Fog is commonly found below inversion caps on Earth today. While rich in cloud water, the fog layer is vertically thin, extending through only the bottom ~2 model layers. The second, and main, cloud layer lies well above the inversion, where moist convection can again occur, and atmosphere temperatures are sufficiently cool. The moist greenhouse atmosphere, ironically becomes (relatively) dry in the low atmosphere and thus cloud free around the atmospheric temperature maximum of the inversion. With warmer air aloft, the relatively colder surface acts to limit the amount of water vapor that can flux upward from the stable boundary layer. Thus, the warmer overlying layer features low relative humidities and no clouds (Figures 4b–4d). The main cloud deck forms much higher in the atmosphere where temperatures have cooled significantly, once again permitting larger relative humidities and thus condensation. The main cloud deck is thickest where atmosphere temperatures are between ~260 and 270 K. Despite its increasingly high altitude, the main deck remains optically thick and thus has a strong impact on both solar and thermal radiation (Figure 7d). Cloud fractions remain quite low, about 10% for the main cloud deck (Figure 4c). However, the main cloud deck is spatially thick and contains much more water than do present-day clouds (Figures 4d and 7b). At $T_s = 350.5$ K, the planet has double the cloud water column as the present-day Earth. Thus, despite low cloud fractions, the cloud deck can remain highly reflective.

Changes in cloud cover have an important influence on the evolution of climate under the brightening Sun. The global mean water vapor column and thus the clear-sky greenhouse effect rapidly increase at the moist greenhouse transition (Figures 7a and 7c). However, the global mean cloud water column and cloud forcing reach their minimum magnitudes at the transition (Figures 7b and 7d). The greenhouse effect is given by

$$F_{gh} = \sigma T_s^4 - \text{OLR} \quad (4)$$

where σT_s^4 is the thermal radiation emitted by the surface and OLR is the outgoing longwave radiation at the top of the model. Figure 7c considers clear-sky OLR. (Note that the radiative transfer solver assumes an isothermal layer lying above the top of the model with a pressure thickness equal to that of the pressure at the top interface). Figure 1c illustrates that the cloud albedo reaches a minimum value precisely at the moist greenhouse transition, where the climate sensitivity is greatest. Thus, the abrupt warming of climate found at +12.5% S_0 is aided by a decrease in cloud cover. However, once past the moist greenhouse transition, this trend reverses. Once onto the moist greenhouse branch (i.e., $T_s \geq 331.9$ K), the cloud water column, cloud albedo, and net cloud forcing all sharply increase in magnitude for progressively hotter

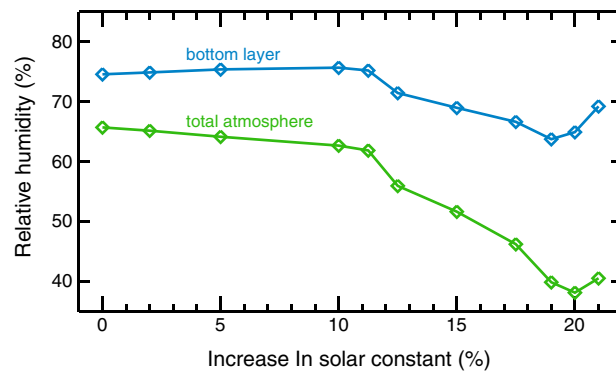


Figure 8. Global mean relative humidity in the bottom most layer of the atmosphere and for the total atmosphere versus increasing solar constant. The total atmosphere relative humidity is the percentage of water vapor by mass contained in the whole atmosphere compared with the water vapor mass the atmosphere could theoretically hold if saturated everywhere.

atmospheres (Figures 1c, 7b, and 7d). Qualitatively similar cloud behavior was recently reported for warming climates using a single-column model with an active hydrological cycle [Popp *et al.*, 2015].

Changes in clouds are related to changes in the convective properties of the atmosphere as it warms. Cloud cover reaches its minimum upon the initial collapse of boundary layer convection (Figures 3d, 4d, and 4e), the mechanism for which is described in section 3.2. However, a moist greenhouse atmosphere is fundamentally different, heated from aloft rather than from below (i.e.,

the ground) as is found for cooler climates. Above the inversion, the atmosphere again permits convection, first dry and then moist. Solar radiation-absorbed aloft provides the energy to drive upper level convection, well above the inversion (Figures 3b and 6). As climate grows progressively hotter, radiative heating aloft becomes stronger, deepening upper level convection (Figures 3c, 3d, and 4e). There is no shortage of water vapor in a moist greenhouse (Figure 2b). Thus, upper level convective overturning can feed copious amounts of moisture into the high atmosphere where it can sufficiently cool, condense, and form clouds (Figures 4d and 6b). As a moist greenhouse matures, the primary cloud deck thickens, thus helping delay the immediate onset of a runaway greenhouse. We postulate that the main cloud deck thickens along the moist greenhouse branch of climate due to increased radiative heating aloft, which in turn drives upper level convective overturning and creates the primary cloud deck.

Figure 8 shows that the relative humidity of the bottom layer of the atmosphere and of the total atmosphere both decline as climate warms. The sharpest decline is found upon the first onset of the moist greenhouse. Subsaturations of the atmosphere is well documented to act against the water vapor greenhouse feedback and thus delay immediate onset of a runaway greenhouse [Pierrehumbert, 1994; Goldblatt *et al.*, 2013; Leconte *et al.*, 2013b; Wolf and Toon, 2014a]. However, at +19% S_0 , this trend reverses too as the atmosphere begins to become more humid with increasing T_s and climate sensitivities again begin to creep upward.

3.4. Differences Between Models

Figure 1 shows that there are sizable differences in the evolution of surface temperature for Earth under increasing solar insolation across various models. There are numerous subtle differences between model constructions that surely contribute to the deviations in global mean surface temperature. However, on first order, the differences lie in the treatment of moist physics. Figure 9 shows global mean vertical profiles of temperature, specific humidity, cloud condensate mass mixing ratio, and lapse rate from CAM4 (this study) and LMDG from Leconte *et al.* [2013b]. One can see that the mean surface temperatures are quite close between these two cases ($T_s \approx 331$ K); however, CAM4 has a generally steeper lapse rate. LMDG uses a theoretical analytical solution for the moist adiabatic lapse rate in water-rich atmospheres with forced convective adjustment [Leconte *et al.*, 2013b; Manabe and Wetherald, 1967]. CAM4 determines the atmospheric thermal structure (and thus the lapse rate) prognostically via the combined heating rates from numerous physical and dynamical processes in the model [Neale *et al.*, 2010]. It is difficult to pinpoint which precise processes cause the CAM4 lapse rates to diverge from LMDG. However, lapse rates exceeding the moist adiabat are expected in the real atmosphere. On Earth, presently, the mean tropospheric lapse rate is ~ 6.5 K/km, which is steeper than the moist adiabat. The lapse rate is influenced not only by moist convection but also equally by baroclinic eddies [Stone and Carlson, 1979]. Thus, a prognostic determination of the lapse rate may be more appropriate than relaxing to the moist adiabat.

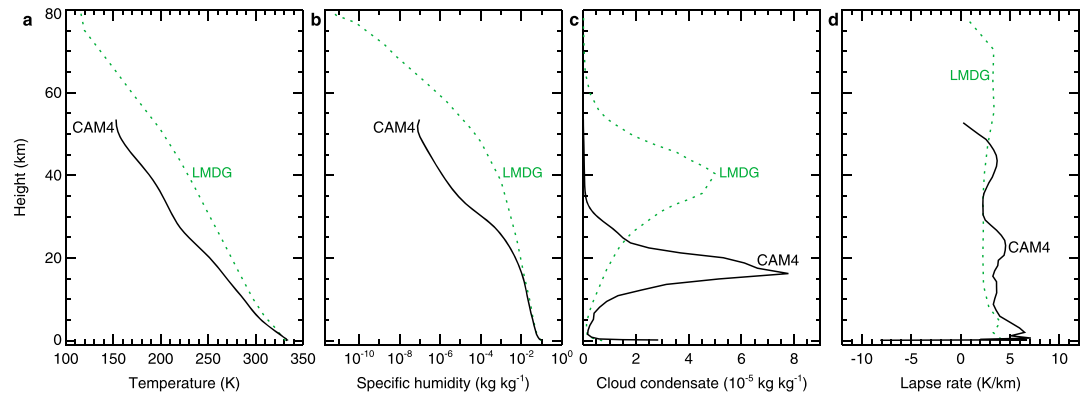


Figure 9. Global mean vertical profiles of (a) temperature, (b) specific humidity, (c) cloud condensate mixing ratio, and (d) lapse rate for CAM4 and LMDG simulations with (nearly) the same surface temperature (~ 331 K).

With a warmer upper atmosphere, LMDG can contain more total water vapor than CAM4 despite nearly identical mean surface temperatures (Figure 9b). In both models, the primary cloud deck moves upward in the atmosphere as climate warms. However, CAM4 tends to form clouds lower in the atmosphere (~ 17 km versus ~ 40 km), at warmer temperatures (~ 265 K versus ~ 230 K), and also of greater peak cloud water concentrations (~ 8 kg kg $^{-1}$ maximum versus ~ 5 kg kg $^{-1}$ maximum) compared with LMDG simulations of approximately equal mean surface temperature (Figure 9). Clouds that form at relatively higher temperatures will favor reflectivity over the greenhouse effect and thus contribute more strongly toward cooling the planet. Differences in the temperature of cloud formation between LMDG and CAM4 likely control the differences found in net cloud forcing.

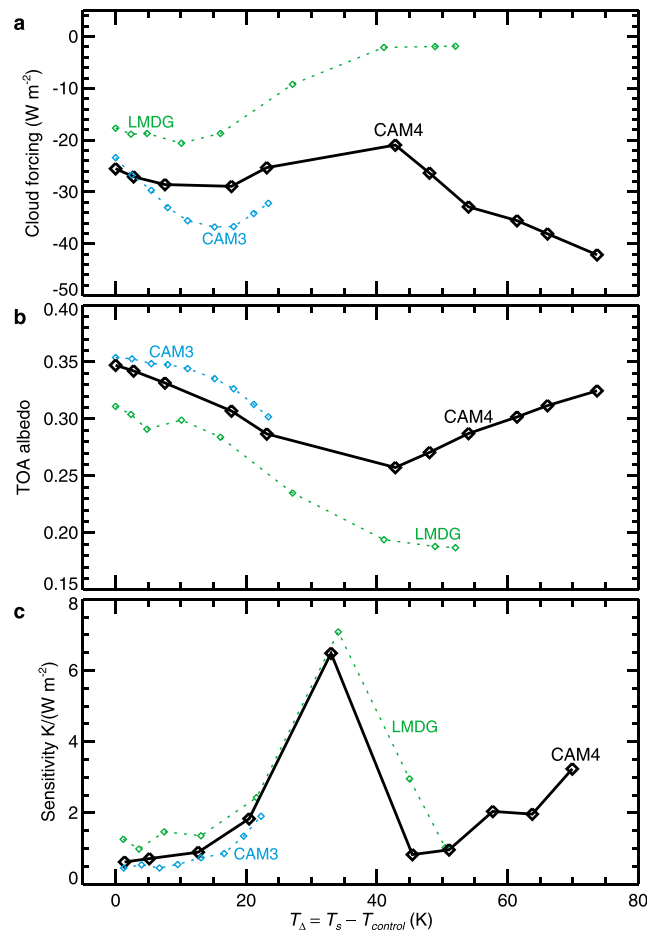


Figure 10. (a) Global mean cloud forcing, (b) top-of-atmosphere albedo, and (c) climate sensitivity versus mean surface temperature. Data are labeled as in Figure 1.

We next consider quantities as a function of global mean surface temperature instead of solar constant, because surface temperature is the dominant control on the amount of water vapor that enters the atmosphere. Water vapor and temperature combine to control clouds. Plotted in temperature space, patterns among the models are clearly visible. Figure 10 shows the global mean net cloud forcing, the TOA albedo, and the climate sensitivity as a function of the global mean surface temperature above that of the control simulation given by

$$T_{\Delta} = T_s - T_{\text{control}} \quad (5)$$

CAM3 simulations reach only $T_{\Delta} \approx +23$ K due to the onset of numerical instabilities (see section 2.4). LMDG enters a classical runaway greenhouse state with

a last stable mean surface temperature of $T_{\Delta} \approx +52$ K. CAM4 simulations reach up to $T_{\Delta} \approx +74$ K before numerical instabilities are encountered (see section 3.1).

As T_{Δ} increases to +40 K, all three models show qualitative similarities. Net cloud forcings initially become stronger (i.e., more negative) before weakening as T_{Δ} exceeds +15 K (Figure 10a). TOA albedos decrease in all models as a result of both changing cloud forcings and increased solar absorption by water vapor (Figure 10b). Climate sensitivities for CAM4 and LMDG achieve maximum values at nearly the same T_{Δ} while CAM3 sensitivity closely follows that of CAM4 until its crash point. Note that similar to Figure 1b, in Figure 10c, the climate sensitivity is plotted on a staggered x coordinate grid, located at the midpoint of each incremental change in surface temperature.

While qualitative similarities in the evolution of clouds and climate sensitivity are indeed encouraging, their differences in magnitude cause diverging mean climate states (Figure 1a). CAM3 is slightly cloudier than CAM4. Stronger net cloud forcing in CAM3 leads to TOA albedos that are ~1–7% larger than in CAM4. CAM3 climate sensitivity follows that of CAM4 quite closely in temperature space. However, CAM3 clouds grow thicker, faster with increasing temperature (Figure 10a), such that the CAM3 climate sensitivity is always a bit less than that of CAM4 (Figure 10c). Lower sensitivity means that it takes longer (i.e., a higher solar constant) for CAM3 to evolve to a given mean surface temperature as seen in Figure 1a.

LMDG has a significantly weaker cloud forcing compared with CAM4 (Figure 10a). This is true for control simulations and becomes more dramatic as climate warms. The TOA albedos of LMDG are consistently ~11–29% lower than found in CAM4. The net cloud forcing in LMDG changes more rapidly with increasing temperatures, essentially vanishing for $T_{\Delta} \geq +40$ K with a value of about -2 W m^{-2} . CAM4 simulations also indicate weakening cloud forcing up through $T_{\Delta} = +40$ K; however, the effect is far smaller. The minimum magnitude value for net cloud forcing for CAM4 is -20.9 W m^{-2} found at $T_{\Delta} = +42.8$ K. At this surface temperature, the net cloud forcing in CAM4 is an order of magnitude stronger than found in LMDG. As T_{Δ} grows even larger, LMDG cloud forcings remain constant, while CAM4 cloud forcings reverse their trend and begin to grow stronger (more negative), increasing the TOA albedo and helping stabilizing climate against a runaway.

For both LMDG and CAM4, on first order, the sharp transition to a moist greenhouse by $T_{\Delta} \approx +40$ K is caused by the water vapor greenhouse feedback. However, in each model, different moist physical processes are responsible for enhancing climate sensitivity at the transition. In LMDG, inversions cannot form due to assumptions regarding the lapse rate; thus, presumably no shut off of convective surface cooling can occur, as it does in CAM4. However, in LMDG, changes to clouds strongly destabilize climate as a moist greenhouse is approached (Figure 10a). In CAM4, the destabilizing effect of clouds near the transition is present but is significantly weaker than is found with LMDG. However, in CAM4, the shut off of convective surface cooling due to inversions contributes significantly to warming climate (Figure 3d). Once the moist greenhouse state is reached, climate sensitivities fall for both models. For $T_{\Delta} \geq +40$ K, clouds cease to be a destabilizing force, leveling off in LMDG while growing thicker in CAM4. In CAM4, reductions to convective surface cooling also again become gradual past the transition. While the spike in climate sensitivity found in LMDG and CAM4 has a common root cause and a similar magnitude, important differences remain within the respective moist physical calculations.

Model intercomparison is essential for forwarding the art of climate modeling. While intercomparison projects are already widely used for problems of modern climate, it may be more critical for studies of theoretical exoplanetary atmospheres where no observations exist with which to constrain our models. Here we have discussed first-order differences between the models but have not thoroughly examined the physical parameterizations causing this to be so. Further work is warranted to compare the details of physical parameterizations, including radiative transfer, clouds, and convection, for hot climates across various three-dimensional climate models.

3.5. Limiting Fluxes

The concept of a limiting value for the outgoing longwave radiation (OLR) from a clear-sky, saturated, hot, water-rich atmosphere is well established. The latest theoretical calculations place this limit at 282 W m^{-2} [Goldblatt *et al.*, 2013]. If the absorbed solar radiation (ASR) exceeds this limit, a runaway greenhouse will occur. Here clear-sky radiative fluxes (both OLR and ASR) exceed the theoretical flux limit described in

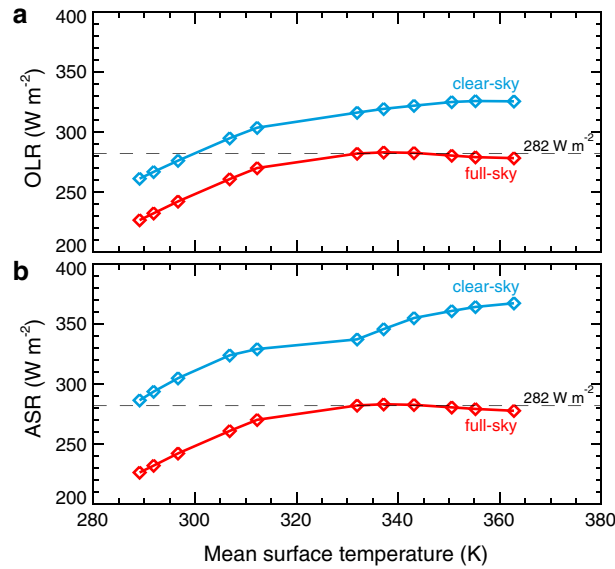


Figure 11. (a) Global mean outgoing longwave radiation (OLR) and (b) absorbed solar radiation (ASR) versus mean surface temperature. The radiation limit of Goldblatt *et al.* [2013] is labeled at 282 W m^{-2} . The difference between full-sky and clear-sky radiation equals the longwave and shortwave cloud forcings.

The theoretical underpinning for radiation flux limits for clear-sky atmospheres is strong, but the picture becomes more complex for cloudy atmospheres. Clouds add significantly to both the solar reflectivity and the thermal opacity of the atmosphere. For moist greenhouse atmospheres, high clouds become more latitudinally uniform than in cooler atmospheres (Figures 4c and 4d). Regions of subsaturation (i.e., low relative humidity) become overlain by a thick layer of clouds (Figures 4b and 4d). Clouds are highly effective greenhouse agents; thus, the main cloud deck can block low relative humidity longwave radiative windows to space. With sufficiently thick and extensive clouds decks, the temperature of the clouds becomes an additional limiting factor on OLR.

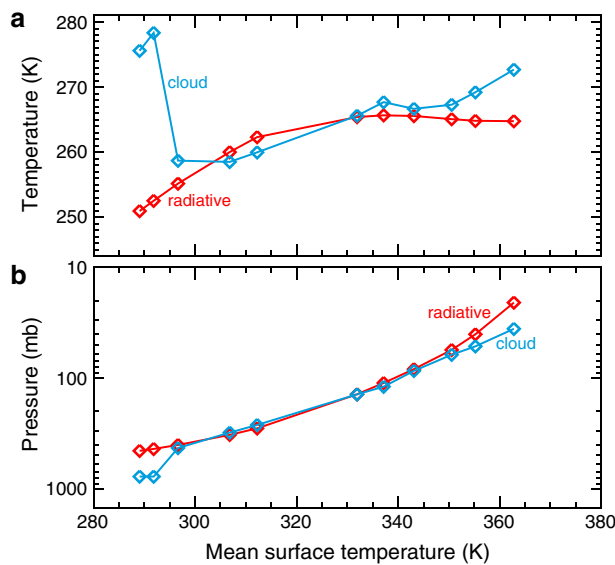


Figure 12. The global and annual mean radiation to space temperature and pressure (red) and the temperature and pressure where cloud condensate mixing ratios reach a maximum in the atmosphere (blue).

Goldblatt *et al.* [2013] (Figure 11). However, this behavior is fully expected as our simulations feature significantly subsaturated atmospheres (Figures 4b and 8). A subsaturated atmosphere can have OLR that exceeds the radiation limit because the water vapor greenhouse effect is made less intense by subsaturation. Note that a radiation limit still exists for subsaturated atmospheres, but it becomes larger for increasing subsaturation. However, when we also consider the radiative effect of clouds (i.e., full sky), we find a peculiar phenomenon. OLR and ASR appear to approach the radiation limit of Goldblatt *et al.* [2013] but only via modulation by clouds (Figure 11). This limiting behavior is seen once the moist greenhouse climate is reached at $T_s \geq 331.9 \text{ K}$.

Figure 12 shows that the global and annual mean radiation to space temperature and pressure and the temperature and pressure at which the global mean cloud condensate mixing ratio reach its maximum. The radiation to space temperature is calculated as

$$T_{\text{space}} = (\text{OLR}/\sigma)^{1/4}, \quad (6)$$

where σ is the Stefan-Boltzmann constant. The radiation to space pressure is the level at which the atmospheric temperature equals T_{space} . For moist greenhouse atmospheres T_{space} asymptotes to $\sim 265 \text{ K}$; however, the radiation to space level moves steadily upward (lower pressure) as climate warms. As is described in Goldblatt and Watson [2012], emission to space occurs approximately where the optical depth is equal to one. For hot climates ($T_s \geq 330 \text{ K}$ in this study),

the temperature structure around the emission to space level follows the moist adiabat (Figure 5). As surface temperatures increase further, the temperature structure at the emission to space level remains unchanged, and thus the amount of radiation that can be emitted to space reaches a limiting value.

Maxima in the global mean cloud condensate mixing ratio remain between 258 and 278 K despite a ~ 74 K range in mean surface temperatures. For our control and $+2\%$ S_0 simulations, the maximum in cloud condensate mixing ratio lies just above 800 mbar and at atmospheric temperatures of 275 and 278 K. For warmer climates, the maximum in cloud condensate mixing ratio more closely follows the radiation to space level and temperature. Due to the dependence of the saturation specific humidity on ambient pressure, the temperature at which clouds form increases slightly as the pressure of formation decreases.

Taken in isolation, the greenhouse effect of clouds would cause a thermal runaway to occur under less solar insolation. Despite continually rising T_s and clear-sky OLR that asymptotes to $\sim 326 \text{ W m}^{-2}$, longwave cloud forcings limit full-sky OLR to $\leq 282 \text{ W m}^{-2}$ (Figure 11a). However, the main cloud layer remains sufficiently thick as to still contribute strongly to the planetary albedo. Clear-sky ASR continually rises; however, strengthening shortwave cloud forcing ensures that the full-sky ASR is kept in balance with OLR and thus limited to $\leq 282 \text{ W m}^{-2}$ (Figure 11b). Once the full-sky OLR reaches its limiting value, all increases to the solar constant (and therefore surface temperature) are accompanied by sharp increases (more negative) in the shortwave cloud forcing in order to maintain equilibrium against a thermal runaway (Figures 7d and 10a). Despite their high altitude, upper level clouds in the moist greenhouse can strongly affect solar radiation due to their considerable optical thickness.

3.6. Sensitivity to Water Cycle Parameters

In this study we have demonstrated stable moist greenhouse atmospheres in a 3-D climate model. This climate state features a distinctive shift in radiative, convective, and cloud properties compared with that of the modern atmosphere. Climate models notoriously rely on tunable parameters within subgrid-scale convection and cloud schemes, and CAM4 is no exception. Thus, we have conducted sensitivity tests for seven subgrid-scale cloud and convection parameters. While this is by no means a comprehensive exploration of the parameter space, we test those that are expected to most heavily influence modeled climate [Covey *et al.*, 2013]. As a baseline case, we chose the simulation with $+17.5\%$ S_0 and $T_s = 343.1$ K, representing a typical moist greenhouse atmosphere. We then vary pertinent water cycle parameters to their minimum and maximum plausible values as defined by Covey *et al.* [2013]. Our results are presented in Table 1.

First, the moist greenhouse appears to be a robust result against plausible changes to water cycle parameters. All simulations presented in Table 1 feature the distinctive radiative-convective state described in section 3.2. We find that the moist greenhouse is generally insensitive to parameters controlling convection. This is not surprising since convection is generally muted in the moist greenhouse. However, parameters controlling clouds tend to have a more significant effect on climate. Again, this is no surprise, as here our default atmosphere ($+17.5 S_0$, $T_s = 343.1$ K) has almost double the total cloud water column than does the present-day Earth (Figure 7b). Thus, changes to cloud tunings have an amplified effect on the climate of a moist greenhouse. The model demonstrates its greatest sensitivity to the minimum relative humidity threshold for high clouds (cldfrc_rhminh) and to the liquid cloud droplet effective radius (rliq). Changing cldfrc_rhminh directly modulates the primary cloud deck of a moist greenhouse which is typically located above 200 mbar. The effective radius of liquid droplets is well known to significantly impact climate. Here there is no exception. Changing rliq by a mere $\pm 40\%$ has the largest effect on climate (-10.1 K and $+14.2$ K, respectively). This is a significantly greater sensitivity to changing liquid cloud droplet radii than is found by Wolf and Toon [2014b] for Archean climates with $T_s \approx 288$ K and high CO_2 .

4. Discussion

4.1. Escape of Water to Space

Moist greenhouse atmospheres can become prone to water loss. If water vapor remains a significant constituent of the atmosphere up to high altitudes, photolysis followed by hydrogen escape can

Table 1. Sensitivity Tests for Important Water Cycle Parameters Applied to a Moist Greenhouse Atmosphere^a

Case	Surface Temperature (K)	TOA Albedo	TOA Upwelling LW Flux (W m ⁻²)	Net Cloud Forcing (W m ⁻²)	Greenhouse Effect (W m ⁻²)
Default moist greenhouse (+17.5% S_0)	343.1	0.287	282.7	-32.9	507.3
Minimum relative humidity threshold for low stable clouds (0.9)					
cldfrc_rhminl = 0.80	339.6	0.287	283.4	-34.0	474.5
cldfrc_rhminl = 0.99	345.9	0.288	282.1	-31.9	533.8
Minimum relative humidity threshold for high stable clouds (0.8)					
cldfrc_rhminh = 0.65	334.3	0.306	275.4	-34.5	436.0
cldfrc_rhminh = 0.85	352.7	0.286	283.2	-30.5	599.4
Liquid cloud droplet effective radius (8–14 μ m)					
rliq = default * 0.6	333.0	0.289	282.5	-35.2	418.0
rliq = default * 1.4	357.3	0.298	280.5	-30.9	649.4
Threshold for conversion of cold ice to snow (9.5e-6 kg kg ⁻¹)					
cldwat_icritc = 2.0e-6	341.7	0.281	284.6	-32.4	491.9
cldwat_icritc = 18.0e-6	343.9	0.288	281.6	-32.3	515.7
Minimum overshoot parameter for shallow convection (0.1)					
hkconv_betamn = 0.02	341.5	0.288	282.3	-33.4	492.6
hkconv_betamn = 0.3	343.5	0.288	282.2	-33.1	511.8
Characteristic time scale for shallow convection (1800 s)					
hkconv_cmftau = 900	342.7	0.286	283.1	-32.4	503.2
hkconv_cmftau = 14400	342.4	0.318	270.0	-36.8	512.8
Characteristic time scale for deep convection (3600 s)					
zmconv_tau = 1800	342.8	0.279	286.1	-31.4	501.4
zmconv_tau = 28800	347.7	0.297	278.1	-31.1	555.2

^aDefault parameter values are shown in parentheses in column 1. The greenhouse effect is calculated via equation (4).

irreversibly remove water from the planet. Here we consider diffusion-limited escape as is frequently done in moist greenhouse literature. For a light-weight minor constituent such as H, the escape rate can be approximated by

$$\Phi(H) \approx bf(H)/H_s \quad (7)$$

where b is the binary Brownian diffusion coefficient, $f(H)$ is the hydrogen mixing ratio, and H_s is the scale height at the top of model [Hunten, 1973]. Here we assume that the hydrogen mixing ratio, $f(H)$, is equal to twice the H₂O mixing ratio found at the model top ($p_{\text{top}} \sim 0.2$ mbar). The binary diffusion coefficient is approximated by that of H in Earth air via the parameterization

$$b = 6.5 \times 10^{17} T_{\text{top}}^{0.7} \quad (8)$$

where T_{top} is the temperature at the top of the model [Hunten, 1973]. We use global mean values for the temperature and H₂O volume mixing ratio at the model top. Our calculation provides an upper bound on hydrogen escape rates as we neglect bottlenecks that may exist above our 0.2 mbar model top. Hydrogen loss rates could also be reduced if escape becomes energy limited [Watson et al., 1981].

Here, only simulations under +19%, +20%, and +21% S_0 are subject to appreciable water loss, having Q_{top} equal to 2.0×10^{-3} and 1.1×10^{-2} and 5.6×10^{-2} , respectively. Following equations (7) and (8) and assuming that the present-day ocean has 1.4×10^{24} g of water, equaling 2×10^{28} atoms cm⁻² of hydrogen, we can estimate how long it takes to remove all water from Earth via diffusion-limited escape. For simulations +19%, +20%, and +21% S_0 , the entirety of Earth's oceans could evaporate in as little as ~ 3.5 Gyr, ~ 672 Myr, and ~ 130 Myr given a static climate. However, more detailed calculations of atmospheric water loss from moist greenhouse atmospheres are warranted.

4.2. The Fate of Earth

The evolution of solar luminosity over time can be approximated by the equation of *Gough* [1981]

$$L(t) = \left[1 + \frac{2}{5} \left(1 - \frac{t}{t_0} \right) \right]^{-1} L_0 \quad (9)$$

where t is the time relative to the present, t_0 is the present age of the Earth (~ 4.6 Gyr), and L_0 is the present-day solar luminosity. In our simulations, stable climates can be maintained at $+21\%$ S_0 and $T_s = 362.8$ K. Following equation (9), this value of S_0 will occur ~ 1.99 Gyr from today. However, such an atmosphere could lose its water in as little as ~ 130 Myr. In that time, the Sun will have increased another $\sim 2\%$ in brightness. The climatological stability of moist greenhouse atmospheres along with rapid H escape rates implies that Earth may lose its oceans before a thermal runaway can take place. Complete loss of Earth's oceans may occur in little over 2 Gyr, transforming Earth into a desert planet. After the last of Earth's water vanishes, carbon-silicate weathering will shut down as water is needed for sequestering CO_2 . CO_2 will then accumulate in the atmosphere through natural volcanic outgassing until Earth presumably resembles Venus.

While extremophiles may survive on Earth until (and possibly after) the loss of the oceans ~ 2 Gyr from now, surface habitability for humans will end far sooner. The human body is unable to physiologically adapt to sustained hot temperatures, with lethal hyperthermia setting in when wet bulb temperatures (T_{wb}) exceed 310 K for extended periods [Sherwood and Huber, 2010]. Here our simulation at $+11.25\%$ S_0 has global mean T_{wb} in the lowest model layer over land of 302.6 K. While extremes of temperature may locally exceed the hyperthermia limit proposed by Sherwood and Huber [2010], sustained surface habitability would likely be maintained on large parts of the planet. However, once Earth transitions to a moist greenhouse at $+12.5\%$ S_0 , global mean T_{wb} over land rises to 323.4 K and remains above the hyperthermia limit everywhere. At this point, ~ 1.3 Gyr in the future, humans will not be able to physiologically survive, in nature, on Earth.

4.3. Relevance to the Habitable Zone

Based on *Kepler Space Telescope* surveys, it is estimated that 22% of Sun-like stars have Earth-sized planets orbiting in their habitable zone (HZ) [Petigura et al., 2013]. Planets around solar-type stars may also have the best chance of containing Earth-like water endowments [Tian and Ida, 2015]. Kasting et al. [1993] and Kopparapu et al. [2013] both use the moist greenhouse threshold to delimit the inner edge of the HZ. Kasting et al. [1993] argue that the inner edge of the HZ should be set where a planet will lose its entire inventory of water within the lifetime of the planet. Given diffusion-limited hydrogen escape, this threshold corresponds to upper atmosphere H_2O volume mixing ratios of $\geq 10^{-3}$. In this work, our $+19\%$ S_0 simulation will lose the entirety of Earth water inventory in ~ 3.5 Gyr given a constant climate. This time frame is less than half the expected lifetime of our solar system. Thus, in the traditional context of exoplanetary habitability, $+19\%$ S_0 (equivalently 1619.91 W m^{-2} solar insolation) marks the inner edge of the HZ around the Sun via the water loss limit. Converting to distance, the inner edge of the HZ for Earth in our solar system presently can be set at a distance of 0.92 AU. But human life cannot survive sustained surface temperatures greater than 310 K, well below that of a moist greenhouse. Here this threshold is exceeded at $+12.5\%$ S_0 (equivalently 1531.43 W m^{-2} solar insolation). Thus, for our solar system, the inner edge of the HZ for human life is currently 0.94 AU. For comparison, LMDG sets the inner edge of the HZ via a runaway greenhouse at 0.95 AU with no moist greenhouse occurring [Leconte et al., 2013b]. One-dimensional simulations of Kopparapu et al. [2013] set the inner edge of the HZ via the water loss limit at 0.99 AU and via a runaway greenhouse at 0.97 AU.

These limits all apply to water-rich planets, where there is thus no constriction on the water vapor greenhouse feedback. However, desert planets can potentially maintain habitable surface temperatures at larger solar insolutions than used here because water is scarce, and thus, the water vapor greenhouse is muted [Abe et al., 2011]. On such planets, moist and runaway greenhouses would never occur. A water-rich planet that undergoes a moist and/or runaway greenhouse could transition into a desert planet after severe water loss. After the last of the planet's water is lost from the surface, continuing water loss to space would reduce atmospheric H_2O mixing ratios, causing temperatures to fall until H_2O escape rates lessened sufficiently, allowing a new equilibrium climate to emerge. Thus, a water-rich planet could experience an additional period of habitability, reborn as a relatively cooler desert planet after the heat of a moist greenhouse has subsided.

4.4. The Merits of 3-D

While 3-D climate models enjoy widespread use for problems concerning the present-day Earth, only recently have they risen to prominence for modeling planetary and exoplanetary atmospheres. Simulations of moist and runaway greenhouses have long been the domain of 1-D radiative-convective equilibrium models. While 1-D models can be tuned to provide reasonable answers for rapidly rotating planets, still they often miss or must oversimplify critical pieces of physics. Many notable results have come from 1-D models that assume cloud-free skies, fully saturated atmospheres, forced convective adjustment to the moist adiabat, and isothermal 200 K stratospheres. As we have discussed in this work, hot climates are critically described by their hydrological cycle. Preconceived assumptions regarding such climates may be incorrect.

Three-dimensional models can help rectify many of these issues by providing interactive hydrological calculations. Temperature, water vapor, relative humidity, clouds, and their collective radiative effects are all self-consistently included. While 1-D models are now beginning to loosen their long-held assumptions on lapse rate [Wordsworth and Pierrehumbert, 2013] and include refined convection and cloud schemes [Zsom et al., 2012; Popp et al., 2015], 1-D models fundamentally cannot capture the large-scale dynamics of the atmosphere. Large-scale dynamics dictate the spatial distribution of clouds and relative humidity on Earth, both of which interact strongly with the radiation fields. For instance, dry columns form in hot climates in both CAM4 and LMDG. These dry columns are coincident with the subsiding branches of the Hadley circulation and provide important low-relative humidity windows where energy can escape to space. Furthermore, cloudy regions of the atmosphere are typically coincident with storm tracks, another fundamentally 3-D aspect to climate.

5. Summary

In this study we have simulated the climate of Earth under increasing solar insolation using a three-dimensional climate model. In our simulations, Earth transitions into a moist greenhouse when the solar constant is increased by 12.5% above the present day. At this point, Earth abruptly warms by ~20 K for only a 1.25% incremental increase in the solar constant. A switch in the radiative-convective properties of the atmosphere accompanies the switch into a moist greenhouse climate state. Moist greenhouse atmospheres feature net radiative heating of the near-surface layers due to large thermal and solar opacities from large atmospheric water vapor inventories. This heating creates inversions that effectively shut off boundary layer convection. Thus, the surface of a moist greenhouse can neither cool radiatively nor convectively, triggering abrupt warming. However, once past this transition, climate is able to stabilize against the immediate onset of a thermal runaway. While the near-surface atmosphere remains hot, dry, and stagnant, above the inversion convection can again occur, feeding moisture into extensive upper level cloud decks. These cloud decks remain sufficiently thick as to contribute strongly to the planetary albedo, helping stabilize climate. Diffusion-limited water loss becomes significant in our simulations when the solar constant is increased by 19%, with mean surface temperatures of 350.5 K and H₂O volume mixing ratios of 2×10^{-3} at the model top at ~0.2 mbar. We find climatologically stable states with the solar constant raised by 21%, with mean surface temperatures of 362.8 K and H₂O volume mixing ratios of 5.6×10^{-2} at the model top. However, at this point, diffusion-limited water loss may become rapid, such that the entirety of Earth's oceans is lost within ~130 Myr. Thus, the death of Earth will likely be at the hands of the moist greenhouse, not a thermal runaway. We conclude that habitability on Earth for water-based life will be irreversibly terminated no later than ~2.1 Gyr from today. However, physiological constraints on the human body imply that Earth will become uninhabitable for humans in ~1.3 Gyr.

Acknowledgments

We thank NASA Planetary Atmospheres Program award NNN13ZDA001N-PATM and NASA Exobiology Program award NNX10AR17G for financial support. This work utilized the Janus supercomputer, which is supported by the National Science Foundation (award CNS-0821794) and the University of Colorado at Boulder. We thank R.K. Kopparapu, J. Haqq-Misra, J. F. Kasting, J. Yang, and D. Abbot for their helpful discussions. We thank C. A. Shields for providing the updated numerical solver for the deep convection scheme. We thank D. Abbot, C. Goldblatt, and C. McKay for their thoughtful reviews of this manuscript. CESM1.2 is freely available to all at <http://www.cesm.ucar.edu/models/cesm1.2/> via the National Center for Atmospheric Research, Boulder, CO. Modeling results and the radiative transfer code used in this study can be obtained by contacting eric.wolf@colorado.edu.

References

- Abe, Y., A. Abe-Ouchi, N. H. Sleep, and K. J. Zhanle (2011), Habitable zone limits for dry planets, *Astrobiology*, 11(5), 443–460.
- Allen, C. (1973), *Astrophysical Quantities*, Univ. of London, Athlone Press, London.
- Bitz, C. M., K. M. Shell, P. R. Gent, D. A. Bailey, G. Danabasoglu, K. C. Armour, M. M. Holland, and J. T. Kiehl (2012), Climate sensitivity of the Community Climate System Model, version 4, *J. Clim.*, 25, 3053–3070.
- Borysow, A., and L. Frommhold (1986), Theoretical collision-induced rototranslational absorption spectra for modeling Titan's atmosphere: H₂ – N₂ pairs, *Astrophys. J.*, 303, 495–510.
- Brent, R. P. (1973), *Algorithms for Minimization Without Derivatives*, Prentice Hall, Englewood Cliffs, N. J.

- Clough, S. A., M. W. Shephard, E. J. Mlawer, J. S. Delamere, M. J. Iacono, K. Cady-Pereira, S. Boukabara, and P. D. Brown (2005), Atmospheric radiative transfer modeling: A summary of the AER codes, *J. Quant. Spectros. Radiat. Transfer*, **91**, 233–244.
- Covey, C. D. D., J. Lucas, X. G. Tannahill, and R. Klein (2013), Efficient screening of climate model sensitivity to a large number of perturbed input parameters, *J. Adv. Model. Earth Syst.*, **5**, 598–610.
- Donahue, T. M., J. H. Hoffman, R. R. Hodges, and A. J. Watson (1982), Venus was wet: A measurement of the ratio of deuterium to hydrogen, *Science*, **216**, 630–633.
- Evans, D. A., N. J. Beukes, and J. L. Kirshvink (1997), Low-latitude glaciation in the Proterozoic era, *Nature*, **386**, 262–266.
- Goldblatt, C., and A. J. Watson (2012), The runaway greenhouse: Implications for future climate change, geoengineering and planetary atmospheres, *Philos. Trans. R. Soc. London, Ser. A*, **370**, 4197–4216.
- Goldblatt, C., T. D. Robinson, K. J. Zahnle, and D. Crisp (2013), Low simulated radiation limit runaway greenhouse climates, *Nat. Geosci.*, **6**, 661–667.
- Goldblatt, C. (2015), Habitability of waterworlds: Runaway greenhouses, atmospheric expansion, and multiple climate states of pure water atmospheres, *Astrobiology*, **15**(5), 362–370.
- Gough, D. O. (1981), Solar interior structure and luminosity variations, *Sol. Phys.*, **74**, 21–34.
- Guinan, E. F., and I. Ribas (2002), Our changing Sun: The role of solar nuclear evolution and magnetic activity on Earth's atmosphere and climate, in *The Evolving Sun and its Influence on Planetary Environments*, *APS Con. Ser.*, vol. 269, 85–106, Astronomical Society of the Pacific, San Francisco, Calif.
- Hack, J. J. (1994), Parameterization of moist convection in the National Center for Atmospheric Research Community Climate Model (CCM2), *J. Geophys. Res.*, **99**, 5551–5568, doi:10.1029/93JD03478.
- Halevy, I., R. T. Pierrehumbert, and D. P. Schrag (2009), Radiative transfer in CO₂-rich paleoatmospheres, *J. Geophys. Res.*, **114**, D18112, doi:10.1029/2009JD011915.
- Hofmann, P. F., A. J. Kaufman, G. P. Halverson, and D. P. Schrag (1998), A Neoproterozoic snowball Earth, *Science*, **281**, 1342–1346.
- Hunten, D. M. (1973), The escape of light gases from planetary atmospheres, *J. Atmos. Sci.*, **30**, 1481–1494.
- Ingersoll, A. P. (1969), The runaway greenhouse: Implications for future climate change, geoengineering and planetary atmosphere, *Philos. Trans. R. Soc. London, Ser. A*, **370**, 4197–4216.
- Kasting, J. F. (1988), Runaway and moist greenhouse atmospheres and the evolution of Earth and Venus, *Icarus*, **74**, 472–494.
- Kasting, J. F., J. B. Pollack, and D. Crisp (1984a), Effect of high CO₂ levels on surface temperature and atmospheric oxidation state of the early Earth, *J. Atmos. Chem.*, **1**, 403–428.
- Kasting, J. F., J. B. Pollack, and T. P. Ackerman (1984b), Response of Earth's atmosphere to increases in solar flux and the implications for loss of water from Venus, *Icarus*, **57**, 335–355.
- Kasting, J. F., D. P. Whitmire, and R. T. Reynolds (1993), Habitable zones around main sequence stars, *Icarus*, **101**, 108–128.
- Komabayashi, M. (1967), Discrete equilibrium temperature of a hypothetical planet with the atmosphere and the hydrosphere of a one component-two phase system under constant solar radiation, *J. Atmos. Sci.*, **49**, 2256–2266.
- Kopparapu, R. K., R. Ramirez, J. F. Kasting, V. Eymet, T. D. Robinson, S. Mahadevan, R. C. Terrien, S. Domagal-Goldman, V. Meadows, and R. Deshpande (2013), Habitable zones around main-sequence stars: New estimates, *Astrophys. J.*, **765**, 131, (pp. 16).
- Leconte, J., F. Forget, B. Charnay, R. Wordsworth, F. Selsis, and E. Millour (2013a), The 3-D climate modeling of close-in land planets: Circulation patterns, climate moist bistability and habitability, *Astron. Astrophys.*, **554**, 17.
- Leconte, J., F. Francois, B. Charnay, R. Wordsworth, and A. Pottier (2013b), Increased insolation threshold for runaway greenhouse processes on Earth-like planets, *Nature*, **504**, 268–271.
- Lin, S. J., and R. B. Rood (1996), Multidimensional flux-form semi-Lagrangian transport schemes, *Mon. Weather Rev.*, **124**, 2046–2070.
- Manabe, S., and R. T. Wetherald (1967), Thermal equilibrium of the atmosphere with a given distribution of relative humidity, *J. Atmos. Sci.*, **24**, 241–259.
- Marsh, D. R., M. J. Mills, D. E. Kinnison, J.-F. Lamarque, N. Calvo, and L. M. Polvani (2013), Climate change from 1850 to 2005 simulated in CESM1 (WACCM), *J. Clim.*, **26**, 7372–7391.
- Mlawer, E. J., S. J. Taubman, P. D. Brown, M. J. Iacono, and S. A. Clough (1997), Radiative transfer for inhomogeneous atmospheres: RRTM, a validated correlated-k model for the longwave, *J. Geophys. Res.*, **102**(D14), 16,663–16,682, doi:10.1029/97JD00237.
- Nakajima, S., Y.-Y. Hayashi, and Y. Abe (1992), A study on the runaway greenhouse effect with a one-dimensional radiative-convective equilibrium model, *J. Atmos. Sci.*, **49**(23), 2256–2266.
- Neale, R. B., et al. (2010), Description of the NCAR Community Atmosphere Model (CAM 5.0), *NCAR/TN-486+STR NCAR TECHNICAL NOTE*.
- Petigura, E. A., A. W. Howard, and G. Marcy (2013), Prevalence of Earth-size planets orbiting Sun-like stars, *Proc. Natl. Acad. Sci. U.S.A.*, **110**(48), 19,273–19,278.
- Pierrehumbert, R. T. (1994), Thermostats, radiator fins, and the local runaway greenhouse, *J. Atmos. Sci.*, **52**(10), 1784–1806.
- Pollack, J. B. (1971), A nongrey calculation of the runaway greenhouse: Implications for Venus' past and present, *Icarus*, **14**, 295–306.
- Popp, M., H. Schmidt, and J. Marotzke (2015), Initiation of a runaway greenhouse in a cloudy column, *J. Atmos. Sci.*, **72**, 452–471.
- Ramanathan, V., and J. A. Coakley (1978), Climate modeling through radiative-convective models, *Rev. Geophys. Space Sci.*, **16**(4), 465–489.
- Rasch, P. J., and J. E. Kristjánsson (1998), A comparison of the CCM3 model climate using diagnosed and predicted condensate parameterizations, *J. Clim.*, **11**, 1587–1614.
- Raymond, D. J., and A. M. Blyth (1986), A stochastic mixing model for non-precipitating cumulus clouds, *J. Atmos. Sci.*, **43**, 2708–2718.
- Raymond, D. J., and A. M. Blyth (1992), Extension of the stochastic mixing model to cumulonimbus clouds, *J. Atmos. Sci.*, **49**, 1968–1983.
- Ribas, I. (2009), The Sun and stars as the primary energy input in planetary atmospheres, *Solar and Stellar Variability (IAU S264): Impact on Earth and Planets*, *Proc. Int. Astron. Union*, **5**, 3–18, doi:10.1017/S1743921309992298.
- Richter, J. H., and P. J. Rasch (2008), Effects of convective momentum transport on the atmospheric circulation in the community atmosphere model, version 3, *J. Clim.*, **21**, 1487–1499.
- Schröder, K.-P., and R. C. Smith (2008), Distant future of the Sun and Earth revisited, *Mon. Not. R. Astron. Soc.*, **386**, 155–163, doi:10.1111/j.1365-2966.2008.13022.x.
- Sherwood, S. C., and M. Huber (2010), An adaptability limit to climate change due to heat stress, *Proc. Natl. Acad. Sci. U.S.A.*, **107**(21), 9552–9555.
- Shi, G., N. Xu, B. Wang, T. Dai, and J. Zhao (2009), An improved treatment of overlapping absorption bands based on the correlated k distribution model for thermal infrared radiative transfer calculations, *J. Quant. Spectros. Radiat. Transfer*, **110**, 435–451.
- Simpson, G. C. (1927), Some studies in terrestrial radiation, *Mem. R. Meteorol. Soc.*, **11**, 69–95.
- Stone, P. H., and J. H. Carlson (1979), Atmospheric lapse rate regimes and their parameterization, *J. Atmos. Sci.*, **36**, 415–423.
- Tian, F., and S. Ida (2015), Water contents of Earth-mass planets around M dwarfs, *Nat. Geosci.*, doi:10.1038/NGEO2372.

- Toon, O. B., C. P. McKay, T. P. Ackerman, and K. Santhanam (1989), Rapid calculation of radiative heating rates and photodissociation rates in inhomogeneous multiple scattering atmospheres, *J. Geophys. Res.*, *94*(D13), 16,287–16,301, doi:10.1029/JD094iD13p16287.
- Towe, K. M. (1981), Environmental conditions surrounding the origin and early evolution of life: A hypothesis, *Precambrian Res.*, *16*, 1–19.
- Vardavas, I. M., and J. H. Carver (1984), Solar and terrestrial parameterizations for radiative-convective models, *Planet. Space Sci.*, *32*(10), 1307–1325.
- Watson, A. J., T. M. Donahue, and J. C. G. Walker (1981), The dynamics of a rapidly escaping atmosphere: Applications to the evolution of Earth and Venus, *Icarus*, *48*, 150–166.
- Wolf, E. T., and O. B. Toon (2013), Hospitable Archean climates simulated by a general circulation model, *Astrobiology*, *13*(7), 1–18, doi:10.1089/ast.2012/0936.
- Wolf, E. T., and O. B. Toon (2014a), Delayed onset of runaway and moist greenhouse climates for Earth, *Geophys. Res. Lett.*, *41*, 167–172, doi:10.1002/2013GL058376.
- Wolf, E. T., and O. B. Toon (2014b), Controls on the Archean climate system investigated with a global climate model, *Astrobiology*, *14*(3), 241–253.
- Wordsworth, R. D., and R. T. Pierrehumbert (2013), Water loss from terrestrial planets with CO₂-rich atmospheres, *Astrophys. J.*, *778*, 154 (19pp).
- Young, G. M., V. von Brunn, D. J. C. Gold, and W. E. L. Minter (1998), Earth's oldest reported glaciation: Physical and chemical evidence from the Archean Mozaan group (~2.9 Ga) of South Africa, *J. Geol.*, *106*, 523–538.
- Zhang, G. J., and N. A. McFarlane (1995), Sensitivity of climate simulations to the parameterization of cumulus convection in the Canadian climate centre general circulation model, *Atmosphere–ocean*, *33*(3), 407–446.
- Zsom, A., L. Kaltenegger, and C. Goldblatt (2012), A 1-D microphysical cloud model for Earth and Earth-like exoplanets: Liquid water and water ice clouds in the convective troposphere, *Icarus*, *221*, 603–616.